XV. Spacecraft Data Systems

ASTRIONICS DIVISION

A. Evaluation of Recording Tape and Heads for Spacecraft Magnetic Tape Recorder Applications, *J. K. Hoffman, S. H. Kalfayan,[1] and R. H. Silver[1]*

Phase III of a study of the characteristics of magnetic recording tapes and the tape-to-head interface in the spacecraft environment was completed. The work was performed under direction of the Spacecraft Data Systems Section with facility and personnel support from the Propulsion Division. The results of the work are reported in detail in SPS 37-65, Vol. III, pp. 168–171. Phases I and II were reported in SPS 37-63, Vol. III, p. 160, and SPS 37-64, Vol. III, p. 119, respectively.

Consistent with the objective to optimize the head-to-tape interface, recent work has concentrated on investigation of the effects of varying materials of head fabrication. In this latest work, some previous experiments were repeated employing magnetic heads with Monel metal brackets instead of the brass bracket heads previously used.

These experiments also included examination of the behavior of a surface-treated (Vacoated) sample of a previously tested tape type (3M 20250) to evaluate the effect of the process on the stick-slip and tape-to-head adhesion phenomenon.

The knowledge obtained from this program has been instrumental in understanding and solving the tape-to-head interface problems encountered in development of the *Mariner* Mars 1971 data storage subsystem. It is of significant value relative to the design of data storage subsystems for future missions.

The investigations are continuing and further tests involving additional parameters are planned.

[1]Polymer Research Section, Propulsion Division.

B. The Implementation of *m*-ary Linear Feedback Shift Registers With Binary Devices, *M. Perlman*

1. Introduction

The binary shift register with linear logic (i.e., sum modulo 2 or complement sum modulo 2) feedback has been a subject of serious investigation since 1952. Gilbert, Golomb, Huffman, Zierler, and Peterson (Refs. 1–5) are among the notable contributors. The amenability of the linear (binary) feedback shift register (LFSR) to mathematical description, analysis, and synthesis played a significant role in its development. Mathematical theory for characterizing the LFSR actually preceded the physical existence of the LFSR (Ref. 6). However, diverse applications, coupled with advancing technology, provided underlying motivation in the study of LFSRs [as well as nonlinear FSRs (Ref. 7), which are much less tractable mathematically].

Applications include scaling, counting, prescribed sequence generation, ranging, error-correcting encoders and decoders, secure communication coding, arithmetic operations over a finite field, and load-sharing matrix switching. As noted in Ref. 7, the FSR can be used as a mathematical model for the following:

(1) Random number generators.

(2) Autonomous finite-state machines for research in recursive logic and automata theory.

(3) Markov processes.

Much of the research was confined to the binary FSR because of the availability of reliable two-state devices. Linear p-ary (where p is prime) FSRs have also been treated (Ref. 5). Their behavior is related to the divisibility properties of polynomials over $GF(p)$ ($p = 2$ is a special case). In SPS 37-64, Vol. III, pp. 120–124, and Ref. 8, the m-ary LFSR is shown to be decomposable into parallel p-ary LFSRs.

The m-ary LFSR may be characterized by the linear recurrence relation

$$a_k = \gamma + \sum_{i=1}^{r} c_i\, a_{k-i} \bmod m \qquad (1)$$

The state of the ith stage at clock pulse interval (CPI) k is denoted by a_{k-i}. Each of the r-stages can assume one of m distinct states 0, 1, $\cdots$, $m-1$. The digit fed back at CPI k is a_k, the output of a modulo m summer whose inputs are γ and $c_i a_{k-i}$ over all i, where r and $c_i \in \{0, 1, \cdots, m-1\}$. The state of the ith stage at CPI becomes the state of the $(i+1)$th state at CPI $k+1$. The sequence $\{a_k\} = \{a_0, a_1, a_2, \cdots\}$ for a given initial state $a_{-1}\, a_{-2} \cdots a_{-r}$ is comprised of the coefficients of ascending powers of x of $G_\gamma(x)$, the *generating function*. Expressed in closed form (Refs. 7 and 8),

$$G_\gamma(x) = \frac{\gamma + (1-x)\, g(x)}{(1-x)\, f(x)} \bmod m \qquad (2)$$

where

$$g(x) = \sum_{i=1}^{r} c_i\, x^i \left(a_{-i}\, x^{-i} + a_{-i+1}\, x^{-i+1} + \cdots + a_{-1}\, x^{-1}\right)$$

and

$$f(x) = 1 - \sum_{i=1}^{r} c_i\, x^i$$

2. Implementation of *m*-ary LFSRs with Binary Devices

An m-ary LFSR is first decomposed into p-ary parallel LFSRs where each p is a distinct prime factor of the integer m. The states of a p-ary ($p > 2$) LFSR are coded in binary. The implementation of a p-ary LFSR is comprised of n parallel binary shift registers where $2^{n-1} < p < 2^n$ with *interdependent* binary feedback functions which are in general nonlinear.

Example 1. Given $a_k = 5\, a_{k-1} + a_{k-2} \bmod 6$,

$$G_0(x) = \frac{(5\, a_{k-1} + a_{k-2}) + a_{k-1}\, x}{1 + x + 5\, x^2} \bmod 6$$

The recurrence relation and its associated generating function describe the behavior of the LFSR shown in Fig. 1.

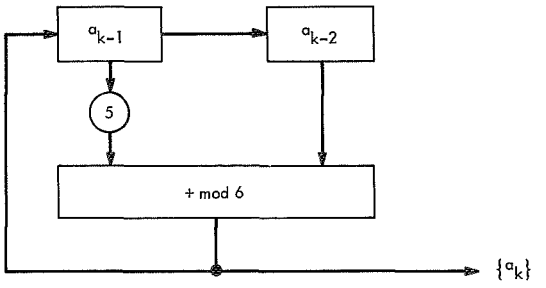

Fig. 1. LFSR characterized by $a_k = a_{k-1} + 5a_{k-2}$ mod 6

By decomposition (Ref. 9, Theorem 5),

$$G_0^2(x) = \frac{(b_{-1} + b_{-2}) + b_{-1}x}{1 + x + x^2} \bmod 2$$

$$G_0^3(x) = \frac{(2d_{-1} + d_{-2}) + d_{-1}x}{1 + x + 2x^2} \bmod 3$$

where

$$b_{-1} = a_{-1} \bmod 2, \qquad b_{-2} = a_{-2} \bmod 2$$
$$d_{-1} = a_{-1} \bmod 3, \qquad d_{-2} = a_{-2} \bmod 3$$

characterize a binary and a ternary LSFR operating in parallel.

$G_0^2(x)$ and $G_0^3(x)$ are associated with the simultaneous recurrence relations

$$b_k = b_{k-1} + b_{k-2} \bmod 2$$

and

$$d_k = 2d_{k-1} + d_{k-2} \bmod 3$$

respectively.

The implementation of the binary LFSR is completely described by the generating function $G_1^2(x)$ and its associated recurrence relation. It appears in Fig. 2. The states in the state table of the ternary LFSR can be represented in binary as follows:

k	d_{k-1}	d_{k-2}	d_k	x_{k-1}	y_{k-1}	x_{k-2}	y_{k-2}	x_k	y_k
0	0	1	1	0	0	0	1	0	1
1	1	0	2	0	1	0	0	1	0
2	2	1	2	1	0	0	1	1	0
3	2	2	0	1	0	1	0	0	0
4	0	2	2	0	0	1	0	1	0
5	2	0	1	1	0	0	0	0	1
6	1	0	1	0	1	1	0	0	1
7	1	1	0	0	1	0	1	0	0
0	0	0	0	0	0	0	0	0	0

The binary representations of d_{k-1} and d_{k-2} are stored $x_{k-1}\ y_{k-1}$ and $x_{k-2}\ y_{k-2}$, respectively. The most significant binary digits reside in the x register. Thus, the ternary LSFR is implemented as two binary registers with *interdependent* Boolean feedback functions which are nonlinear. The feedback functions (i.e., x_k and y_k) appear in Fig. 3 in minimum disjunctive form resulting from using unspecified binary states as "don't cares."

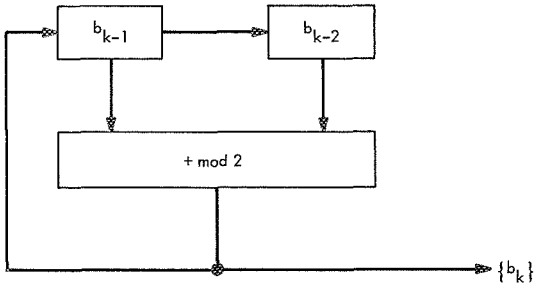

Fig. 2. LFSR characterized by $b_k = b_{k-1} + b_{k-2}$ mod 2

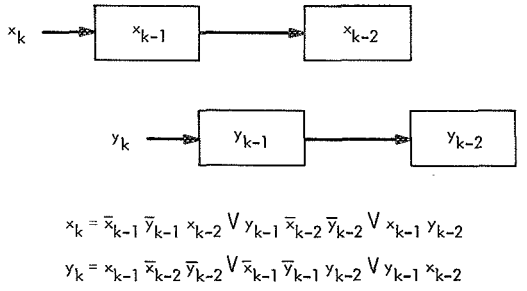

Fig. 3. Implementation LFSR characterized by $d_k = 2d_{k-1} + d_{k-2}$ mod 3 where $d_{k-i} \longleftrightarrow x_{k-i}\ y_{k-i}$ for $i = 0, 1, 2$

A one-to-one correspondence exists between the states $a_{k-1}\,a_{k-2}$ and $b_{k-1}\,b_{k-2}\,x_{k-1}\,y_{k-1}\,x_{k-2}\,y_{k-2}$. Let

$$a_{-1}\,a_{-2} = 0\,2$$

then

$$b_{-1}\,b_{-2} = 0\,0$$
$$d_{-1}\,d_{-2} = 0\,2$$

and

$$x_{-1}\,y_{-1}\,x_{-2}\,y_{-2} = 0\,0\,1\,0$$

The cycle (of states) containing these initial states are

k	a_{k-1}	a_{k-2}	a_k	b_{k-1}	b_{k-2}	x_{k-1}	y_{k-1}	x_{k-2}	y_{k-2}	x_k	y_k
0	0	2	2	0	0	0	0	1	0	1	0
1	2	0	4	0	0	1	0	0	0	0	1
2	4	2	4	0	0	0	1	1	0	0	1
3	4	4	0	0	0	0	1	0	1	0	0
4	0	4	4	0	0	0	0	0	1	0	1
5	4	0	2	0	0	0	1	0	0	1	0
6	2	4	2	0	0	1	0	0	1	1	0
7	2	2	0	0	0	1	0	1	0	0	0

The period 8 associated with a_k (for $a_{-1}\,a_{-2} = 0\,2$) can be determined from the least common multiple (LCM) of the periods of $G_0^2(x)$ and $G_0^3(x)$, namely LCM (1,8) or 8.

Whenever m is a product of distinct primes, as in *Example 1*, a one-to-one correspondence exists between the cycles of m-ary states and the cartesian product of the parallel p-ary states.

Example 2. Given $a_k = 1 + a_{k-1} + 3a_{k-2} \mod 8$, the longest cycle contains $a_{-1}\, a_{-2} = 01$ as an initial state and results in a

$$G_1(x) = \frac{1}{(1-x)(1+7x+5x^2)} \mod 8$$

The period of the longest cycle divides the period associated with

$$G_1^2(x) = \frac{1}{(1-x)(1+x+x^2)^2} \mod 2$$

The period of the m-ary cycle ($m = 8$) is 6 whereas the period associated with $G_1^2(x)$ is 12 (Ref. 9). Decrementing the power of the exponent in the denominator of $G_1^2(x)$ results in the generating function

$$\hat{G}_1(x) = \frac{1}{(1-x)(1+x+x^2)^2} \mod 2$$

with a period of 6 equal to the m-ary cycle. Associated with $\hat{G}_1(x)$ is

$$b_k = 1 + b_{k-2} + b_{k-4} \mod 2$$

There are 10 cycles of length 6, one of length 3, and one of length 1 associated with a_k, whereas there are two cycles of length 6, one of length 3, and one of length 1 associated with b_k. A homomorphic mapping of cycles of states associated with a_k onto those associated with b_k exists. Thus, a binary LFSR characterized by b_k will contain at least one cycle of each length appearing in the m-ary LFSR.

References

1. Gilbert, E. N., *Quasi-Random Binary Sequences,* Memorandum MM-53-1400-42. Bell Telephone Laboratories, Nov. 27, 1953.
2. Golomb, S. W., *Sequences With Randomness Properties,* Final Report, Contract W. 36-039SC-54-36611. Glenn L. Martin Co., Baltimore, Md., 1955.
3. Huffman, D. A., "The Synthesis of Linear Sequential Coding Networks," *Information Theory,* pp. 77–95. Edited by Colin Cherry. Academic Press, New York, 1956.
4. Zierler, N., "Linear Recurring Sequences," *J. Soc. Indust. Appl. Math.*, Vol. 7, pp. 31–48, 1959.
5. Peterson, W. W., *Error-Correcting Codes.* The M.I.T. Press, Cambridge, Mass., 1961.
6. Hall, M., "An Isomorphism Between Linear Recurring Sequences and Algebraic Rings," *Trans. Am. Math. Soc.*, Vol. 44, pp. 196–218, 1938.
7. Golomb, S. W., *Shift Register Sequences.* Holden-Day, Inc., San Francisco, Calif., 1967.
8. Perlman, M., *Pseudonoise Sequence Generation With Three-Tap Linear Feedback Shift Registers.* Technical Report 32-1492; Jet Propulsion Laboratory, Pasadena, Calif., Nov. 1969.
9. Perlman, M., "Cycle Structure Determination of an *M*-ary Linear Feedback Shift Register," in *Proceedings of the Fourth Hawaii International Conference on System Sciences, University of Hawaii, Honolulu, Ha.,* Jan. 1971.

C. Extraction of Complete Subgraphs: Command Prefix Code for TOPS, *N. Deo*

1. Introduction

A method of establishing command word synchronization for the *Viking* 1975 mission was previously suggested by McEliece (SPS 37-61, Vol. III, pp. 48–50). The synchronization is accomplished by transmitting, to the spacecraft command decoder, a binary word (called prefix) sandwiched between the "idle sequence," $\cdots 00000 \cdots$, and the actual command word. The prefix acts as the word-start signal and synchronizes the command decoder. As pointed out by McEliece, the criterion for selecting a prefix is that it should be a shortest possible sequence capable of being recognized by the command decoder even if the prefix (as well as the preceding idle sequence) has been corrupted (up to a certain pre-specified extent) by the noisy channel.

2. Command Decoding in the TOPS

A similar approach is proposed for the thermoelectric outer planet spacecraft (TOPS), with one important difference. Because of extremely long mission life, unknown and hostile environments, and long transmission distances, the spacecraft is expected to have several redundant command decoders. The central computer subsystem will also serve as a command decoder (Ref. 1). It is, therefore, proposed that the prefix, in addition to being an error-correcting synchronizer, also identify the specific command decoder for which the command word following the prefix is intended. In other words, the prefixes will act as combinations to unlock specified information-processing channels on the spacecraft. This requires a set of different prefixes, each corresponding to a unique command decoder. Depending on which of the command decoders the ground wishes to use, the corresponding prefix would be transmitted. The prefixes must, of course, be at more than a certain specified Hamming distance from each other because of the noisy channel, etc. A pair of prefixes that satisfies this distance requirement may be called *mutually compatible*. It can be shown that *mutual compatibility is a symmetric, non-reflexive, non-transitive, binary relation.* It can, therefore, be represented by a simple (i.e., free of self-loops and parallel edges) undirected graph.

Thus, the problem of finding a dictionary with the largest possible number of mutually compatible prefixes of a given length and with specified properties with respect to the idle sequence can be reduced to a graph-theoretic problem.

3. Graph-Theoretic Definitions

Since the basic graph-theoretic concepts are fundamental to this problem, the following definitions are presented for those unfamiliar with graph theory. (The reader is directed to Refs. 2 and 3 for a more thorough presentation.)

A *graph* consists of a finite set of points (called *vertices*) and a finite set of line-segments (called *edges*) joining pairs of these points. A graph is said to be *simple* if no edge joins a vertex to itself (i.e., no *self-loop* allowed) and no two edges join the same pair of vertices (i.e., no *parallel edges* allowed). A simple graph is said to be *complete* if there is exactly one edge between every pair of vertices. A simple graph of n vertices has $n(n-1)/2$ edges. A *walk* is an alternating sequence of vertices and edges beginning and ending with vertices in which an edge joins the vertices preceding and following the edge. A *path* is a walk in which no vertex appears twice. A graph is said to be *connected* if there is some path between every pair of vertices. A largest connected subgraph in an unconnected graph is called a *component*. A vertex v in a connected graph G is called *articulation vertex* or *cut-vertex* if removing v (together with all edges incident on v) leaves the remaining subgraph unconnected. An *adjacency matrix* A of graph G with n vertices is an n by n (0,1) matrix, whose i,jth ($=j,i$th) entry is 1 if there is an edge joining vertices i and j; otherwise the i,jth entry is 0. The number of edges incident at a vertex is called the *degree* of a vertex. A vertex of degree one is called a *pendant* vertex.

4. An Example

The problem can be best explained with an example. Assume, for this example, that the length of each prefix is seven bits and that a prefix is required to be at least single-error correcting. Therefore, the Hamming distance between a prefix and all of its shifts (with zeroes filled in at the left) should be at least three. For instance, a 7-bit word $b_1\ b_2\ b_3\ b_4\ b_5\ b_6\ b_7$ and its shifted version by two 0 0 $b_1\ b_2\ b_3\ b_4\ b_5$ must be different in at least three positions. Since the idle sequence consists of all zeroes, a prefix must not start with zero, i.e., $b_1 = 1$.

It is not difficult to write a program for generating all 7-bit words, satisfying the constraints just pointed out. Such a program turned out a list of 33 words, each 7 bits long (out of a possible $2^7 = 128$ words).

To obtain a largest set of mutually compatible words, we generate a graph G in which a vertex represents a

prefix word, and if two prefixes are compatible, an edge is drawn between the corresponding pair of vertices. Clearly, a pendant vertex (or a vertex of degree 1) in G represents a prefix which is compatible with only one other prefix. Since we are searching for codes with more than two prefixes, we can immediately delete all pendant vertices. This results in a graph G_1 of 21 vertices, as shown in Fig. 1. The following are 21 prefixes, corresponding to the 21 vertices in G_1:

1	1	1	1	1	0	1
1	1	1	1	0	1	1
1	1	1	0	1	1	1
1	1	1	0	1	0	0
1	1	1	0	0	1	1
1	1	1	0	0	1	0
1	1	1	0	0	0	1
1	1	0	1	1	1	1
1	1	0	1	1	1	0
1	1	0	1	1	0	0
1	1	0	1	0	1	1
1	1	0	1	0	1	0
1	1	0	1	0	0	1
1	1	0	1	0	0	0
1	1	0	0	1	1	1
1	1	0	0	1	0	1
1	1	0	0	1	0	0
1	1	0	0	0	1	0
1	0	1	1	0	1	0
1	0	1	1	0	0	0
1	0	1	0	1	1	0

The vertices in Fig. 1 are labeled with the octal equivalent of the corresponding 7-bit words.

A largest complete subgraph (usually there is more than one largest complete subgraph in a graph) *in G_1 is the largest possible dictionary of mutually compatible prefixes* we have been looking for. It turns out that in this graph there are no complete subgraphs of more than three vertices. Moreover, the graph contains eight different complete subgraphs of three vertices (called K_3). One such dictionary, for example, consists of the following three words: {(1110111), (1100100), (1011010)}. Thus, with 7-bit, single-error-correcting prefixes, we can have up to three different command decoders.

Similarly, searching for a code of 8-bit prefixes with single-error-correcting capability, one finds that (out of a possible 2^8 words), graph G consists of 87 vertices and G_1 of 85. The largest complete subgraphs in G_1 consist

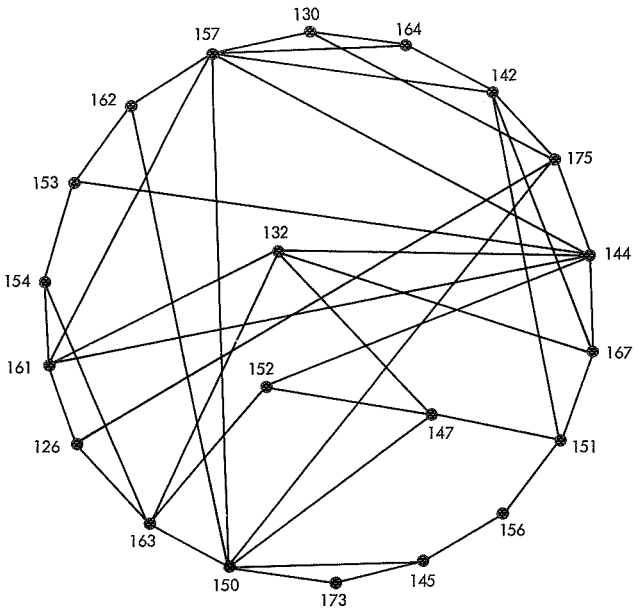

Fig. 1. Graph G_1 of 7-bit, 1-bit error-correcting prefixes

of five vertices (K_5); this allows a maximum of five command decoders.

5. Graph-Theoretic Algorithms

Developing an efficient algorithm for identifying (and thus extracting) all largest complete subgraphs in a given graph is of central importance here. (The futility of combinational brute force in trying to find all compatible words among 85 words taking three at a time, four at a time, and so forth, is obvious.) Algorithms available for computerized graph-theoretic operations are presently few and far between (Refs. 4 and 5).

There are several ways of representing graphs for computer storage and manipulation (Ref. 4); in this case, the adjacency matrix was used.

If a graph is unconnected, it is inefficient to manipulate the entire subgraph in looking for largest subgraphs, because no complete graph can have vertices in two different components of an unconnected graph. Therefore, G_1 must be first checked for connectedness. Each component should be identified and looked at separately, if G_1 is unconnected.

Similarly, since an articulation vertex (or cut vertex) cannot belong entirely to any one complete subgraph (except for the trivial cases of K_1 and K_2), a connected component of G_1 should be checked for separability. If separable, the graph should be broken into its different

blocks and then each block should be searched for the largest complete subgraph.

Thus, the connectedness and separability algorithms are essential subalgorithms for extraction of complete subgraphs. The details of different algorithms and programs for identification of all largest complete subgraphs in a connected, nonseparable graph are being prepared.

The programs were written in APL/360 and run on a time-shared terminal connected to an IBM 360/50.[1]

[1]The author gratefully acknowledges the contribution of Harold Baugh, the cognizant engineer for the TOPS command decoder subsystem, who originally suggested this problem and helped in writing the programs.

References

1. Martin, B. D., "Data Subsystems for 12-Year Mission," *Astronaut. Aeronaut.*, Vol. 8, No. 9, p. 56, Sep. 1970.

2. Harary, F., *Graph Theory*. Addison-Wesley Publishing Co., New York, 1969.

3. Berge, C., *The Theory of Graphs and Its Applications*. John Wiley & Sons, Inc., New York, 1962.

4. Read, R. C., "Teaching Graph Theory to Computer," in *Recent Progress in Combinations*, pp. 161–173. Edited by W. T. Tutte. Academic Press, New York, 1969.

5. Read, R. C., "Graph Theory Algorithms," in *Graph Theory and Its Applications*, pp. 51–78. Edited by B. Harris. Academic Press, New York, 1970.

D. Jupiter's Electron Dose Calculations on Metal Oxide Semiconductor Structures,

S. P. Li and J. B. Barengoltz

1. Introduction

Experimental data of radiation doses on metal oxide semiconductor field-effect transistors (MOSFETs) in the literature are usually reported in terms of rad (Si). For electron irradiation, laboratory energies of several keV, 1 MeV, and 3 MeV are common and, in some cases, up to 20 MeV (Ref. 1). The relative radiation damage may be studied experimentally by using equal electron fluences of different energies, but the experiments become more difficult as the energy is increased. As an additional complication to adequate testing, a MOSFET device inside a spacecraft is not directly irradiated by electrons as in the laboratory, but by the electrons which penetrate a certain thickness of the spacecraft wall with reduced energy plus the ensuing gamma rays. Since the radiation damage on MOSFETs is dominantly due to ionization (with the creation of new surface states causing a flat-band shift being secondary [Ref. 2]), a measure of the energy deposited in the insulator layer of a MOSFET is a direct measure of its ionization damage. In this paper, approximate calculations are performed and reported on the relative weights of damages produced by electrons of different energies with particular reference to the Jupiter radiation belt. Once this is accomplished, a model electron environment, in the form of a fluence-energy distribution, is integrated to yield the overall dose. Considerations discussed in this paper provide a means to obtain direct damage assessments from laboratory measurements corresponding to one particular energy.

A similar situation is found in assessing the total dose that might be received by an astronaut. The difference is that here we are concerned with the insulator material instead of human tissue. With respect to the Jupiter mission, we have chosen to deal with electrons because the total integrated fluxes of neutrons and the gamma rays from inside the spacecraft (due to the radioisotope thermoelectric generators) are of secondary importance (Ref. 3 and footnote 1). The proton damage is more

easily assessed (but is not necessarily smaller) and is deferred because there are presently great uncertainties of its prediction around Jupiter.[1]

2. Method of Calculation

Calculations are made on the following assumptions:

(1) A uniform monoenergetic electron stream of "large" extent and kinetic energy E_0 is incident normally on the spacecraft magnesium wall of thickness t, from which electrons of mean kinetic energy E_0' and photons of certain energy distribution emerge in the same direction and hit normally a composite Al-Si plate of thickness x_1 in Al and x_2 in silicon. In the treatment of a beam of infinite extent, the neglect of angular scattering underestimates the effect of shielding. Therefore, this assumption will lead to a conservative estimate of the dose.

(2) Silicon is used to simulate the silicon dioxide (SiO_2) layer of the MOSFET. Since their densities are almost equal (2.33 and 2.27, respectively) and SiO_2 is predominately silicon, SiO_2 is assumed to have the same electron stopping powers and photon cross-sections as silicon, for which data are readily available.

On the basis of the above, calculations of the dose per unit incident electron fluence can be broken down in the following sequence of steps, with some appropriate assumptions added:

a. Step 1. Consider one electron of a uniform beam of kinetic energy E_0 passing a magnesium plate of thickness t. The mean energy E_0' of the emerging electron is found by an interpolation procedure from range-energy data for Al (Ref. 4) and is taken as that of an emerging mono-energetic beam. Range straggling is taken into account by assigning a probability of transmission for the incident electron of energy E_0 through the magnesium. Thus, an incident electron fluence of energy E_0 is assumed to degrade to a fluence with energy E_0' and a smaller value, decreased by the transmission factor. Values of this factor, as given by Perkins (Ref. 5), are unity for all except very small values of E_0.

b. Step 2. After the effect on the electrons due to the aluminum metallization layer is neglected compared to the magnesium layer, the dose absorbed by the silicon due to the transmitted electrons is calculated. This calculation is standard; the collision stopping power for Al (Ref. 4) was employed. The absorption of energy in the silicon due to bremsstrahlung occurring in the silicon is neglected.

c. Step 3. Next, differential cross-sections are calculated for bremsstrahlung, which occurs as the result of the electrons losing energy by radiation in penetrating the magnesium wall. The formulas used are labelled 3BN and 3BS(e) (originally due to Schiff in Ref. 6) in the review paper of Koch and Motz (Ref. 7), for initial electron energies of 1 MeV and higher than 1 MeV, respectively. The significant assumptions involved are the Born approximation, which is valid for

$$\frac{2\pi Z}{137\beta} \ll 1$$

and the approximation in electron angle integration (not accurate for $\phi_0 \leq Z^{1/3}/111E_0$). Due to the relatively low value of Z (12) and the relativistic electron energies we are dealing with, the above assumptions are justified. In addition, photon-electron showers in the magnesium layer have been neglected because its thickness is much smaller than one radiation length (> 10 cm for Mg) (Ref. 8).

The quantity of interest at this stage of the calculation is the number of photons $N(k)dk$ in the energy interval k and $k + dk$, given by

$$N(k)dk = \frac{d\sigma}{dk} nt\, dk \tag{1}$$

where

$\frac{d\sigma}{dk}$ = bremsstrahlung cross-section, differential with respect to photon energy k, in units of square centimeters per atom per incident electron per MeV

n = number of atoms/cm^3 of material

t = thickness of material, cm

Since $d\sigma/dk$ is a function of the electron energy, the cross-section will, therefore, depend on the depth in the magnesium wall, at which the bremsstrahlung is produced. Since the electron enters with kinetic energy E_0 and leaves with a mean energy E_0', an approximate $d\sigma/dk$ can be evaluated corresponding to electron kinetic energy

$$\frac{E_0 + E_0'}{2}$$

[1]Private communication between N. Divine and J. Barengoltz.

which is applied only for that part of the magnesium in which the electron kinetic energy has not degraded below 0.1 MeV. This adjustment will be unnecessary for $E_0 > 30$ MeV since $E'_0 \approx E_0$, while for $E_0 < 30$ MeV, it provides a correction.

One remark about the attenuation of the photons in the magnesium material is in order. The energy absorption coefficients μ (Ref. 9) are high *only* for low energy photons. For photon energies $k > 0.1$ MeV and assuming even a thickness of 500 mils (magnesium) the transmission factor $e^{-\mu t}$ is never smaller than 0.99. For $k < 0.03$ MeV, however, μ increases rapidly and total attenuation is approached (e.g., for $k = 0.01$ MeV, $e^{-\mu t} \approx e^{-40}$). Therefore, the lower end of the photon spectrum can be neglected in evaluating the effect of the photons on the silicon dioxide layer although the energy absorption coefficients are high for low photon energies. This point is in fact utilized by the establishment of a lower limit on the numerical integration over k.

d. Step 4. The bremsstrahlung dose on the silicon layer can be calculated after the photon distribution $N(k)$ is obtained in Step 3. Since photons are absorbed in both the Al and Si layers, it is obvious that the energy absorbed in the Si layer due to N photons of energy k MeV is given by

$$E_{\text{brem}}(k) = k\,N(k)\exp(-\mu_{\text{Al}}\,x_1)(1 - \exp[-\mu_{\text{Si}}\,x_2]).$$

$$\approx k\,N(k)\,(1 - \exp[-\mu_{\text{Si}}\,x_2]). \qquad (2)$$

The factor $\exp(-\mu_{\text{Al}}\,x_1)$ is taken as unity because x_1 is sufficiently small (approximately 6000 Å) to make this a good approximation for all but the very low energy photons, which have already been neglected in Step 3.

The approximate form of Eq. (2) is multiplied by a suitable factor to convert to dose and the integration over k is carried out by the trapezoidal approximation.

e. Step 5. As a result of Steps 2 and 4, the total dose absorbed by the silicon due to an incident unit electron fluence of energy E_0 on the magnesium can be obtained by an addition of the direct electron and the bremsstrahlung contributions. In this paper, these contributions are not combined, so that their relative effects can be discussed. At this point, instead, an electron model for Jupiter's trapped radiation belts is introduced. The design levels for electron fluence due to Jupiter are based on the spectrum[2]

$$\frac{d\phi}{dE} = 1.5 \times 10^9\, E\, e^{-E/20.1}, \text{ electrons/cm}^2\text{-s-MeV} \qquad (3)$$

A proper treatment of this isotropic flux in terms of the parallel beam assumption would result in a reduction by possibly as much as a factor of 2π. The neglect of this factor adds another measure of conservatism to the estimate. The total dose received by a MOS device in the design level electron environment can now be calculated.

f. Numerical results. The results of calculations are presented for magnesium thicknesses of $t = 50$, 100, 200, and 500 mils, an aluminum thickness $x_1 = 6000$ Å, and silicon thickness $x_2 = 2000$ Å. Initial electron energies of 1, 3, 10, 30, and 100 MeV are used.

g. Electron collision dose. Table 1 summarizes the values of initial electron energy E_0, the reduced energy

[2]Divine, T. N., *The Planet Jupiter (1970)*, NASA Space Vehicle Design Criteria (Environment) Monograph (to be published).

Table 1. Values of E_0, $E'_0(t, T)$, and E_{coll}

E_0, MeV	$E'_0(t, T)$, MeV	E_{coll}, MeV × 10^{-5}
1	0.531 (t = 50 mils, T = 0.65)	4.94
	0 (t = 100 mils, T = 0)	0
	0 (t = 200 mils, T = 0)	0
	0 (t = 500 mils, T = 0)	0
3	2.41 (t = 50 mils, T = 1)	7.18
	2.04 (t = 100 mils, T = 0.96)	6.84
	1.12 (t = 200 mils, T = 0.57)	4.03
	0 (t = 500 mils, T = 0)	0
10	9.40 (t = 50 mils, T = 1)	7.88
	8.82 (t = 100 mils, T = 1)	7.82
	7.68 (t = 200 mils, T = 1)	7.77
	4.45 (t = 500 mils, T = 1)	7.48
30	29.14 (t = 50 mils, T = 1)	8.43
	28.28 (t = 100 mils, T = 1)	8.41
	23.18 (t = 200 mils, T = 1)	8.33
	22.05 (t = 500 mils, T = 1)	8.31
100	98.22 (t = 50 mils, T = 1)	8.93
	96.44 (t = 100 mils, T = 1)	8.92
	94.66 (t = 200 mils, T = 1)	8.91
	83.56 (t = 500 mils, T = 1)	8.87

E_0' of the electrons after passing through a magnesium layer of thickness t, the corresponding transmission factor T, and E_{coll}, the energy per electron deposited in the silicon (2000 Å) by its collisions.

The energy deposited in a slab of silicon, as given in Table 1, is presented graphically in Fig. 1 as a function of magnesium thickness t and incident electron energy E_0. Also note that the intercepts on the vertical axis in Fig. 1 suggest that for zero shielding, electron-induced ionization is fairly unchanged over a wide incident energy range. This conclusion is borne out by experimental data on several ionization sensitive MOSFETs, where the induced degradation for a given fluence of electrons was insensitive to their energies in the range 4 to 20 MeV (Ref. 1).

The results of the direct dose calculation are presented in Fig. 2 where, for simplicity, only two curves are drawn corresponding to $t = 50$ mils (A) and $t = 500$ mils (B). The curves represent a folding of the electron spectrum of Eq. (3) and the dose-thickness dependence of Fig. 1, for a given thickness. Integration of these curves yields a dose of 1.8×10^4 rad for curve A and 1.7×10^4 rad for curve B.

h. Bremsstrahlung dose. Table 2 summarizes the values of initial electron energy E_0, the thickness t of the magnesium layer, and the resultant dose per unit incident electron fluence. For a given E_0, entries for t are presented only where the dose is non-negligible.

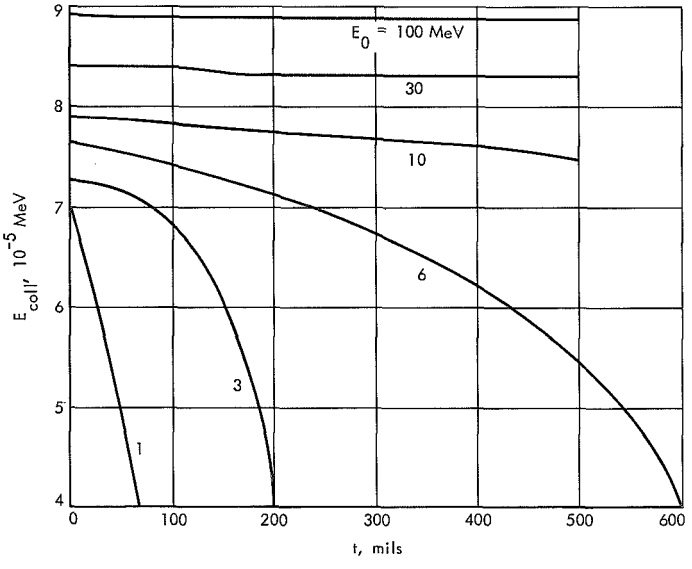

Fig. 1. Energy deposited by electrons in Si after penetrating Mg thickness t

Table 2. Values of initial electron energy, thickness of layer, and dose

E_0, MeV	t, mils	Dose, rad/unit fluence
1	50	1.2×10^{-11}
3	50	1.3×10^{-11}
	100	2.6×10^{-11}
	200	7.4×10^{-12}
10	50	2.7×10^{-11}
	100	5.4×10^{-11}
	200	7.3×10^{-11}
	500	1.6×10^{-10}
30	50	6.9×10^{-11}
	100	1.4×10^{-10}
	200	2.4×10^{-10}
	500	6.0×10^{-10}
100	50	2.5×10^{-10}
	100	5.0×10^{-10}
	200	9.7×10^{-10}
	500	2.4×10^{-9}

The results of Table 2 show that the bremsstrahlung dose increases with increasing electron kinetic energy E_0. They also show that the dose increases linearly with the thickness t of the magnesium shield, as expected

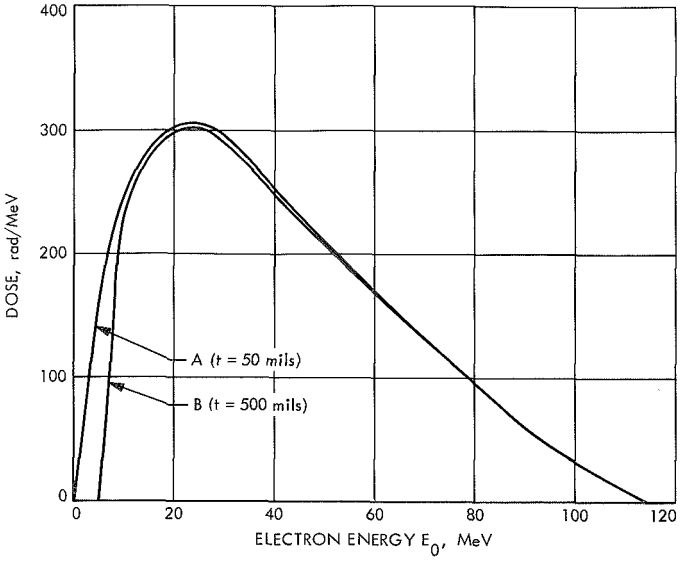

Fig. 2. Differential dose for direct electron collisions, using the spectrum of Eq. (3): curve A is for a 50-mil Mg shield; curve B is for a 500-mil Mg shield

from Eq. (1), until the shield becomes thick enough to significantly attenuate the photons created within it.

As shown in Fig. 3, the differential bremsstrahlung dose has a rather complex form, which is a consequence of folding the electron spectrum (Eq. 3) and the dose-thickness dependence presented in Table 2. For clarity, only the $t = 50$ mils (A) and $t = 500$ mils (B) curves are included. Integration of these curves yields 50 rad and 500 rad, respectively.

3. Conclusions

For currently envisioned outer planet missions, Jupiter's electron-induced ionization dose in MOS structures behind a magnesium wall at least 50 mils thick does not exceed 2×10^4 rad. This dose is near the threshold for degradation of the most ionization-sensitive MOS devices.

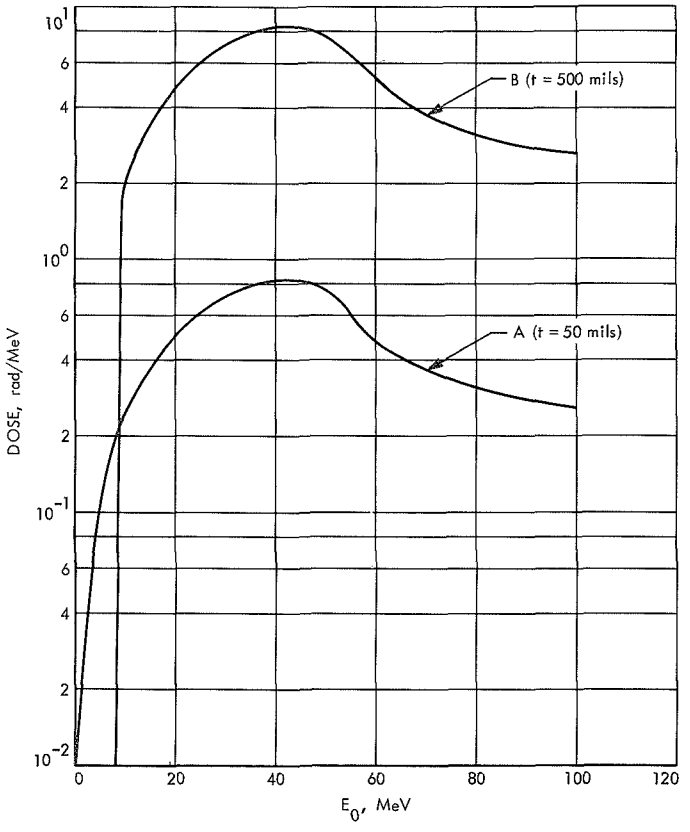

Fig. 3. Differential bremsstrahlung dose, using the spectrum of Eq. (3): curve A is for a 50-mil Mg shield; curve B is for a 500-mil Mg shield

The bremsstrahlung dose is a small part of the total for magnesium walls from 50 to 500 mils thick. Even with a proper treatment of the bremsstrahlung produced in the aluminum layer of a MOS device, estimates show that it is less than 3% of the total dose.

In laboratory testing of MOS devices, where the spacecraft wall shield is absent, 3-MeV electrons are sufficient to simulate the effect of higher energy electrons. In such tests, the weak energy dependence of electron-induced ionization for energies in the range of 3 to 100 MeV may be accurately estimated.

References

1. Palmer, E. E., Miles, J. K., and Lambert, D. L., *Effects of High-Energy Electrons on Candidate Jupiter Probe Electronic Components,* FZM-4910, General Dynamics, 1967.

2. Andre, B., Buxo, J., Esteve, D., and Martinot, H., "Effects of Ionizing Radiation on MOS Devices," *Solid State Electronics,* Vol. 12, pp. 123–131, 1969.

3. Nerman, P. A., Jr., "Low Flux Level Neutron Effects on MOSFET's," *Proc. IEEE Conf. NSRE 16,* 1970.

4. Berger, M. J., and Seltzer, S. M., "Additional Stopping Power and Range Tables for Protons, Mesons, and Electrons," NASA SP-3536, National Aeronautics and Space Administration, Washington, D.C., 1966.

5. Perkins, J. F., "Monte Carlo Calculation of Transport of Fast Electrons," *Phys. Rev.,* Vol. 126, No. 5, p. 1781, 1962.

6. Schiff, L. I., "Energy-Angle Distribution of Thin Target Bremsstrahlung," *Phys. Rev.,* Vol. 83, No. 2, p. 252, 1951.

7. Koch, H. W., and Motz, J. W., "Bremsstrahlung Cross-Section Formulas and Related Data," *Rev. Mod. Phys.,* Vol. 31, No. 4, p. 920, 1959.

8. *The Encyclopedia of Physics,* Reinhold Publishing Corp., p. 85, 1966.

9. Hubbell, L. H., "Photon Cross-Sections, Attenuation Coefficients, and Energy Absorption Coefficients From 10 keV to 100 GeV," NSRDS-NBS 29, National Bureau of Standards, 1969.